Decay of two-dimensional homogeneous turbulence

By J. R. HERRING,

Advanced Study Program, National Center for Atmospheric Research,
Boulder, Colorado 80303

S. A. ORSZAG,

Department of Mathematics, Massachusetts Institute of Technology, Cambridge

R. H. KRAICHNAN

Dublin, New Hampshire 03444

AND D. G. FOX

Meteorological Laboratory, National Environmental Research Center,
Environmental Protection Agency, Research Triangle Park, North Carolina†

The decay of two-dimensional, homogeneous, isotropic, incompressible turbulence is investigated both by means of numerical simulation (in spectral as well as in grid-point form), and theoretically by use of the direct-interaction approximation and the test-field model. The calculations cover the range of Reynolds numbers $50 \leqslant R_L \leqslant 100$. Comparison of spectral methods with finite-difference methods shows that one of the former with a given resolution is equivalent in accuracy to one of the latter with twice the resolution. The numerical simulations at the larger Reynolds numbers suggest that earlier reported simulations cannot be used in testing inertial-range theories. However, the large-scale features of the flow field appear to be remarkably independent of Reynolds number.

The direct-interaction approximation is in satisfactory agreement with simulations in the energy-containing range, but grossly underestimates enstrophy transfer at high wavenumbers. The latter failing is traced to an inability to distinguish between convection and intrinsic distortion of small parcels of fluid. The test-field model on the other hand appears to be in excellent agreement with simulations at all wavenumbers, and for all Reynolds numbers investigated.

1. Introduction

This paper compares theory and computer experiments on the decay of two-dimensional, homogeneous, isotropic, incompressible turbulence. Two analytical theories are studied: (i) the direct-interaction approximation (Kraichnan 1959) and (ii) the test-field model (Kraichnan 1971a, b; Leith & Kraichnan 1972). Numerical solutions for the Navier–Stokes equations are obtained by a variety of accurate methods. Most of the comparisons are made with results obtained by

† Present address: U.S.D.A. Forest Service, Rocky Mountain Forest and Range Experiment Station, Fort Collins, Colorado 80521.

spectral (Fourier) decomposition of the velocity field (Orszag 1971), a method particularly well suited for comparisons with theories like the direct-interaction approximation and test-field model whose form is simplest in the spectral domain. We compare numerical and theoretical results for the evolution of energy and enstrophy (mean-square vorticity) spectra and transfer spectra, as well as spectral integrals like dissipation rates of energy and enstrophy and two-dimensional skewness factors. The present results extend to two dimensions the three-dimensional results of Orszag & Patterson (1972) and Herring *et al.* (1973). In a subsequent paper, we plan to examine the error growth problem in two dimensions, again comparing theory and numerical experiment.

The relevance of idealized two-dimensional turbulence to certain aspects of atmospheric motion has been emphasized in much recent work. Lilly (1971, 1972 a, b) summarizes previous work and relates two-dimensional turbulence to three-dimensional quasi-geostrophic turbulence, the latter being more closely related to atmospheric dynamics (Charney 1971). The goal of the present work is not to pursue these important analogies further, but rather it is to obtain estimates of the accuracy of turbulence theories, as well as to obtain reliable data on two-dimensional turbulence in a range of moderate Reynolds numbers. In this paper, we concentrate on the problem of the decay of turbulence in the absence of external forces, deferring consideration of steady-state turbulence to future work.

The direct-interaction approximation and test-field model are particularly important turbulence models because of their generality, as compared with more *ad hoc* theories like that of Heisenberg (1948). Both the direct-interaction approximation and test-field model apply to a variety of turbulent flows, including homogeneous, shear, and thermal turbulence. [The generalization of the test-field model to inhomogeneous flows has recently been given by Kraichnan (1973).] Of the two theories, the direct-interaction approximation has a sounder logical foundation, as it employs a generalized eddy viscosity which is self-consistently computed in terms of the turbulence energy spectrum with no empirical constants (Herring & Kraichnan 1972; Orszag 1974). The direct-interaction approximation has a well-known defect in treating the interaction of small scales with large scales, viz. the failure of the theory to behave invariantly under *random* Galilean transformations (Kraichnan 1964). This difficulty leads in three dimensions to the prediction by the direct-interaction approximation of a $k^{-\frac{3}{2}}$ inertial-range energy spectrum, instead of the $k^{-\frac{5}{3}}$ Kolmogorov spectrum. In two dimensions, the direct-interaction approximation leads to a $k^{-\frac{5}{2}}$ enstrophy-cascade inertial range instead of the more widely accepted (but still controversial) k^{-3} range. While the inertial-range defect of the direct-interaction approximation is only $k^{\frac{1}{6}}$ in three dimensions, it is $k^{\frac{1}{2}}$ in two dimensions. The numerical results reported in this paper provided some further support for the conclusion that the direct-interaction approximation describes the inertial range worse in two dimensions than in three.

The test-field model is designed to give the proper invariance under random Galilean transformations. The memory times for dynamical interactions in the test-field model are based on the time for loss of coherence of the pressure fluctuations acting on fluid elements. There is a single adjustable parameter λ,

of order one, which affects memory times and, hence, the results of the test-field model. If $\lambda = 0$, the test-field model reduces to the Markovian quasi-normal theory (Orszag 1970), while if $\lambda = \infty$ nonlinear effects vanish and the turbulence executes pure viscous decay. For three-dimensional flow, a λ in the range 1–1·5 appears to give the best comparison with numerical simulations (Herring & Kraichnan 1972).

Two goals of the present paper emerge from the above discussion. (i) Does the inertial-range inadequacy of the direct-interaction approximation imply unsatisfactory predictions of the evolution of the energy-containing region of the spectrum in two dimensions? (ii) What is the best choice for λ in the two-dimensional test-field model?

As mentioned earlier, we believe our numerical simulations to be a reliable source of data on moderate Reynolds number two-dimensional turbulence. An important question is whether large Reynolds number flows with inertial ranges can be realistically simulated with computers at present available. We examine this question in §4 and conclude that the present simulations do *not* have sufficient resolution to simulate properly an inertial range. It is concluded that earlier reports of k^{-3} inertial-range spectra (Lilly 1971, 1972*a*, *b*) and k^{-4} inertial-range spectra (Deem & Zabusky 1971) were premature. However, our conclusions for numerical simulations are not all negative. We have observed a strong degree of Reynolds number independence in the structure of large eddies. Apparently, if one is interested only in the dynamics of enstrophy-containing eddies at large Reynolds numbers, one may get reliable results by simulating the large eddies at moderate Reynolds numbers. This has important consequences for future numerical simulations of turbulence and is discussed at more length later.

In §2, we introduce some notation and concepts useful for the description of two-dimensional turbulence. In §3, we judge the accuracy of various numerical solutions to the two-dimensional Navier–Stokes equations. In §4, we infer what information can be reliably obtained about high Reynolds number turbulence from the present moderate-resolution numerical experiments. In §5, the mathematical formalism of the direct-interaction approximation and test-field model is explained, while in §§6 and 7 we compare the results of the numerical simulations with the theories and give an interpretation of the theoretical significance of the comparisons.

Our results indicate that the direct-interaction approximation satisfactorily predicts the evolution of the energy spectrum at moderate Reynolds numbers. At the highest Reynolds number investigated, the accuracy of the direct-interaction approximation for the energy spectrum and energy-transfer spectrum is inferior to that of the test-field model. For both large and small Reynolds numbers, the direct-interaction approximation gives poor results in the enstrophy dissipation region, as may be expected because of its prediction of an incorrect enstrophy-transfer inertial-range power law. The enstrophy transfer to higher wavenumbers is grossly underestimated by the direct-interaction approximation. An analogous difficulty has been observed in energy transfer in three-dimensional turbulence (Herring *et al.* 1973) and the theoretical explanation for it is similar in two dimensions.

The energy spectrum given by the test-field model with $\lambda = 1$ is in excellent agreement with the present simulations, both at high and low Reynolds numbers. The results are not too sensitive to the value of λ, and satisfactory spectra are obtained with λ ranging from 0·65 to 1, the large wavenumber region being better matched by smaller values of λ than the energy-containing region.

With regard to numerical simulations, our results show that fixed-resolution experiments become inaccurate as the Reynolds number increases. The spectral simulations do not suddenly become inaccurate at all scales; rather, more and more small scales get treated inaccurately with increasing Reynolds number. Enstrophy-containing large-scale motions are treated accurately even at Reynolds numbers two or three times larger than the highest that can be confidently expected to give accurate simulations at all scales. Even more important, our results show a strong degree of Reynolds number independence, as discussed above and in § 4.

2. Formalism and elementary concepts

The flow is assumed to be confined in a cyclic box of side D so that the velocity field may be expanded in the Fourier series

$$\mathbf{v}(\mathbf{x}) = \Sigma \mathbf{u}(\mathbf{k})\, e^{i\mathbf{k}\cdot\mathbf{x}}, \tag{2.1}$$

where the sum extends over wave vectors whose components are integral multiples of $2\pi/D$. In this case the incompressible Navier–Stokes equations become

$$(\partial/\partial t + \nu k^2)\, u_i(\mathbf{k}) = -ik_m(\delta_{ij} - k_i k_j/k^2) \sum_{\mathbf{p}+\mathbf{q}=\mathbf{k}} u_j(\mathbf{p})\, u_m(\mathbf{q}), \tag{2.2}$$

where $k = |\mathbf{k}|$, ν is the kinematic viscosity and incompressibility requires $k_i u_i(\mathbf{k}) = 0$ for all $\mathbf{k}$. In the limit $D \to \infty$, which is necessary for strict isotropy,

$$E(k,t) = \pi k U(k,t,t), \quad U(k,t,t') = \lim_{D\to\infty} (D/2\pi)^2 \langle u_i(\mathbf{k},t)\, u_i(-\mathbf{k},t')\rangle, \tag{2.3}$$

where angular brackets denote an ensemble average and the mean kinetic energy per unit mass is

$$\int_0^\infty E(k)\, dk.$$

$U(k)$ measures the intensity of excitation per mode. The energy balance equation is

$$(\partial/\partial t + 2\nu k^2)\, E(k) = T(k), \quad T(k) = \frac{1}{2}\int_0^\infty \int_0^\infty T(k,p,q)\, dp\, dq, \tag{2.4}$$

where
$$T(k,p,q) = \begin{cases} (4\pi k/|\sin(\mathbf{p},\mathbf{q})|)\,(D/2\pi)^4\,(k_m\,\delta_{ij} + k_j\,\delta_{im}) \\ \times \operatorname{Im}\langle u_i(-\mathbf{k})\, u_j(\mathbf{p})\, u_m(\mathbf{q})\rangle \quad (\mathbf{k} = \mathbf{p} + \mathbf{q}), \\ 0 \quad \text{(if } k, p, q \text{ cannot be the sides of a triangle).} \end{cases} \tag{2.5}$$

The trigonometrical factor in (2.5) arises from the conversion of a two-dimensional integral over wave vectors $\mathbf{p}$ with $\mathbf{q} = \mathbf{k} - \mathbf{p}$ into a $dp\, dq$ integral over the lengths of the sides $\mathbf{p}$ and $\mathbf{q}$ of the triangles formed with $\mathbf{k}$.

Detailed conservation of energy and enstrophy for each triad interaction is expressed by

$$\left.\begin{aligned} T(k,p,q) + T(p,q,k) + T(q,k,p) &= 0, \\ k^2 T(k,p,q) + p^2 T(p,q,k) + q^2 T(q,k,p) &= 0, \end{aligned}\right\} \tag{2.6}$$

which follows from (2.5) by incompressibility. It follows from (2.4) and (2.6) that

$$d\Sigma/dt = -2\nu\Omega \equiv -D, \quad d\Omega/dt = -\eta, \tag{2.7}$$

where $\quad \Sigma = \int_0^\infty E(k)\,dk, \quad \Omega = \int_0^\infty k^2 E(k)\,dk, \quad \eta = 2\nu \int_0^\infty k^4 E(k)\,dk \tag{2.8}$

are the total energy, enstrophy and enstrophy dissipation rate, respectively, and D is the energy dissipation rate. In terms of physical-space quantities,

$$\Sigma = \tfrac{1}{2}\langle|\mathbf{v}|^2\rangle, \quad \Omega = \tfrac{1}{2}\langle|\nabla\times\mathbf{v}|^2\rangle, \quad \eta = \nu\langle|\nabla\times(\nabla\times\mathbf{v})|^2\rangle.$$

It is also useful to introduce certain length scales and non-dimensional parameters of the flow, following in part Lilly (1971). First, the large-scale Reynolds number R_L is defined by

$$R_L = \Sigma/(\nu\eta^{\frac{1}{3}}). \tag{2.9}$$

The length scale associated with (2.9) is

$$L = 1/k_L = \Sigma^{\frac{1}{2}}/\eta^{\frac{1}{3}}, \tag{2.10}$$

which may be interpreted as an integral length scale characteristic of the eddies contributing to total enstrophy.

Second, we define a microscale and associated Reynolds number for two-dimensional turbulence, in analogy with the corresponding three-dimensional definitions, as

$$l = (\nu\Omega/\eta)^{\frac{1}{2}}, \tag{2.11}$$

$$R_l = (l\Omega^{\frac{1}{2}})\,l/\nu = \Omega^{\frac{3}{2}}/\eta \tag{2.12}$$

respectively. The enstrophy dissipation wavenumber (analogous to the Kolmogorov dissipation wavenumber scale in three dimensions) is

$$k_\eta = (\eta/\nu^3)^{\frac{1}{6}}. \tag{2.13}$$

The qualitative theory of the two-dimensional k^{-3} enstrophy-cascade inertial range suggests that $k^4 E(k)$ decays rapidly to zero for $k \gg k_\eta$. Since the enstrophy dissipation spectrum $k^4 E(k)$ behaves like k in the inertial range, the scales of motion that contribute to the enstrophy dissipation rate η, and hence the overall enstrophy dynamics, are $k \lesssim k_\eta$. The modes with $k \gg k_\eta$ have no important effect on modes with $k \lesssim k_\eta$, so that two-dimensional turbulence can be looked upon as a closed dynamical system with appreciable excitation only over the spectral range $0 < k \lesssim k_\eta$. This is the two-dimensional analogue of the fact that three-dimensional turbulence can be considered a closed dynamical system with appreciable excitation only over wavenumbers up to the Kolmogorov dissipation wavenumber.

Two-dimensional turbulence differs essentially from three-dimensional turbulence. In two dimensions, the second conservation law (2.7) implies that enstrophy cannot be created by nonlinear effects, only destroyed by viscosity. Consequently, the rate of energy dissipation in decaying two-dimensional turbulence is bounded by its initial value for all times, since the energy dissipation rate is simply $2\nu\Omega$. On the other hand, in three dimensions enstrophy can be produced by stretching of vortex lines, a process prohibited in two dimensions. The quantity that is

properly analogous to energy dissipation in three dimensions is the enstrophy dissipation in two dimensions. The mean-square vorticity gradient can be increased by nonlinearity in two dimensions, giving rise to enhanced turbulent dissipation of enstrophy.

A two-dimensional skewness factor S_2 can be introduced as a non-dimensional measure of the rate of production of mean-square vorticity gradients by non-linearity. An appropriate definition is

$$S_2 = \int_0^\infty k^4 T(k)\, dk \Big/ \Big[\int_0^\infty k^4 E(k)\, dk \Big(\int_0^\infty k^2 E(k)\, dk \Big)^{\frac{1}{2}} \Big]. \qquad (2.14)$$

S_2 is related to physical-space quantities by

$$S_2 = -2 \Big\langle \frac{\partial v_1}{\partial x} \Big(\frac{\partial \zeta}{\partial x} \Big)^2 \Big\rangle \Big/ \Big[\Big\langle \Big(\frac{\partial v_1}{\partial x} \Big)^2 \Big\rangle^{\frac{1}{2}} \Big\langle \Big(\frac{\partial \zeta}{\partial x} \Big)^2 \Big\rangle \Big], \qquad (2.15)$$

where $\zeta = \partial v_2/\partial x - \partial v_1/\partial y$ is the vorticity. The result (2.15) follows from (2.14), with the use of incompressibility, homogeneity and especially isotropy. Note that the usual (three-dimensional) skewness $S = -\langle (\partial v_1/\partial x)^3 \rangle / \langle (\partial v_1/\partial x)^2 \rangle^{\frac{3}{2}}$ vanishes in two dimensions, as follows from incompressibility and isotropy or from the proportionality of S to the rate of production of energy dissipation (enstrophy) by nonlinearity.

Finally, it is useful to introduce two other parameters which are related to the energy transfer $T(k)$. These are measures of the back transfer of energy to smaller wavenumbers and the transfer of enstrophy to larger wavenumbers. As a measure of back transfer, we take

$$\pi_B = \int_0^{k_s} T(k)\, dk \qquad (2.16)$$

and for forward enstrophy transfer we take

$$\pi_F = \int_{k_l}^\infty k^2 T(k)\, dk. \qquad (2.17)$$

In (2.16), k_s is the smallest positive zero of $T(k)$ and, in (2.17), k_l is the largest finite zero of $T(k)$. At large R_L, $\pi_B(t)$ represents nearly all the energy transferred out of the energy-containing region, the amount transferred to larger wavenumbers becoming vanishingly small as $R_L \to \infty$. Similarly, $\pi_F(t)$ represents, as $R_L \to \infty$, progressively more of the enstrophy transferred out of the enstrophy-containing region. As a dimensionless measure of back transfer we take $\pi_B/2\nu\Omega$; a dimensionless measure of the forward enstrophy transfer is π_F/η.

3. Accuracy of numerical simulations

In two dimensions, it is convenient to solve the Navier–Stokes equations in terms of the vorticity and stream function. With the stream function $\psi(x, y, t)$ related to the velocity by $\mathbf{v} = (\partial \psi/\partial y, -\partial \psi/\partial x)$ and to the (z component of) vorticity by $\zeta(x, y, t) = \partial v_2/\partial x - \partial v_1/\partial y$, the dynamical equations are

$$\partial \zeta/\partial t = \partial(\psi, \zeta)/\partial(x, y) + \nu \nabla^2 \zeta, \qquad (3.1)$$

$$\zeta = -\nabla^2 \psi, \qquad (3.2)$$

where $\partial(f, g)/\partial(x, y)$ denotes the Jacobian of f and g with respect to x and y.

We have solved (3.1) and (3.2) numerically both by spectral methods and by more conventional finite-difference methods. The spectral method is documented elsewhere (Orszag 1971); it involves Fourier-series decomposition of ψ and ζ as in (2.1) with the series truncated after a finite number of terms. The spectral equations for the Fourier coefficients are derived by a projection method like Galerkin's; the resulting equations are analogous to (2.2) in the sense that they involve truncated convolution sums over the wave vectors. These convolutions are most efficiently evaluated using variants of the convolution theorem and fast Fourier transforms. The particular form of the algorithms used for the calculations reported here involves calculation of alias-free convolution sums in ten Fourier transforms per time step as described by Orszag (1971, §6). An alternative algorithm is given by the pseudo-spectral method (Fox & Orszag 1973a), wherein only five Fourier transforms need be performed per time step but aliasing interactions are not removed. We recommend that future spectral calculations be done by the latter, pseudo-spectral method, since it is at least twice as efficient as other spectral methods while giving similar accuracy for similar resolution.

In our comparisons with finite-difference schemes, we used the second-order Arakawa (1966) approximation to the Jacobian in (3.1). Both the Arakawa scheme and the spectral (alias-free) scheme conserve momentum, kinetic energy and enstrophy in the absence of viscous dissipation and time-differencing errors. In all comparisons, time differencing was done by the leapfrog method for the Jacobian term and by lagged explicit differences for the viscous term. Time steps were taken sufficiently small that time-differencing errors may be considered negligible. In the spectral results reported in later sections, the treatment of the viscous term was improved by use of Crank–Nicolson implicit differencing.

We consider the results obtained from 12 different computer runs in order to understand the accuracy and limitations of the various numerical approximations to (3.1) and (3.2). All the runs start from precisely the same initial conditions: a fixed pseudo-random number generator is used to construct a realization of a Gaussian ensemble of two-dimensional incompressible flows with isotropic energy spectrum

$$E(k, t = 0) = v_0^2 (k/k_0) \exp(-k/k_0), \tag{3.3}$$

where $v_0 = 1$ and $k_0 = \frac{3}{2}$. The flow is assumed periodic within a square of side 2π. The 12 runs differ *only* in the viscosity, resolution (number of grid points or modes) and the numerical method (spectral or finite difference). Three choices are made for the viscosity, $\nu = 0.005$, 0.0025 or 0.001; two choices are made for the resolution, either 128×128 or 64×64 (grid points or independent real modes); and two numerical schemes are used, the spectral method and the Arakawa difference scheme. We label the runs so that $F64$ is a finite-difference run with 64×64 resolution, while $S128$ is a spectral run with 128×128 resolution, etc. These run labels relate to the number of independent degrees of freedom in each space direction, not the spectral cut-off wavenumber. The latter is obtained by recalling that an $N \times N$ resolution of $\mathbf{v}$ in physical space (N independent degrees of freedom in each space direction) is completely equivalent to a Fourier representation of $\mathbf{v}$ including all $\mathbf{k}$ with $|k_1| \leqslant \frac{1}{2}N - 1$ and $|k_2| \leqslant \frac{1}{2}N - 1$. Thus the
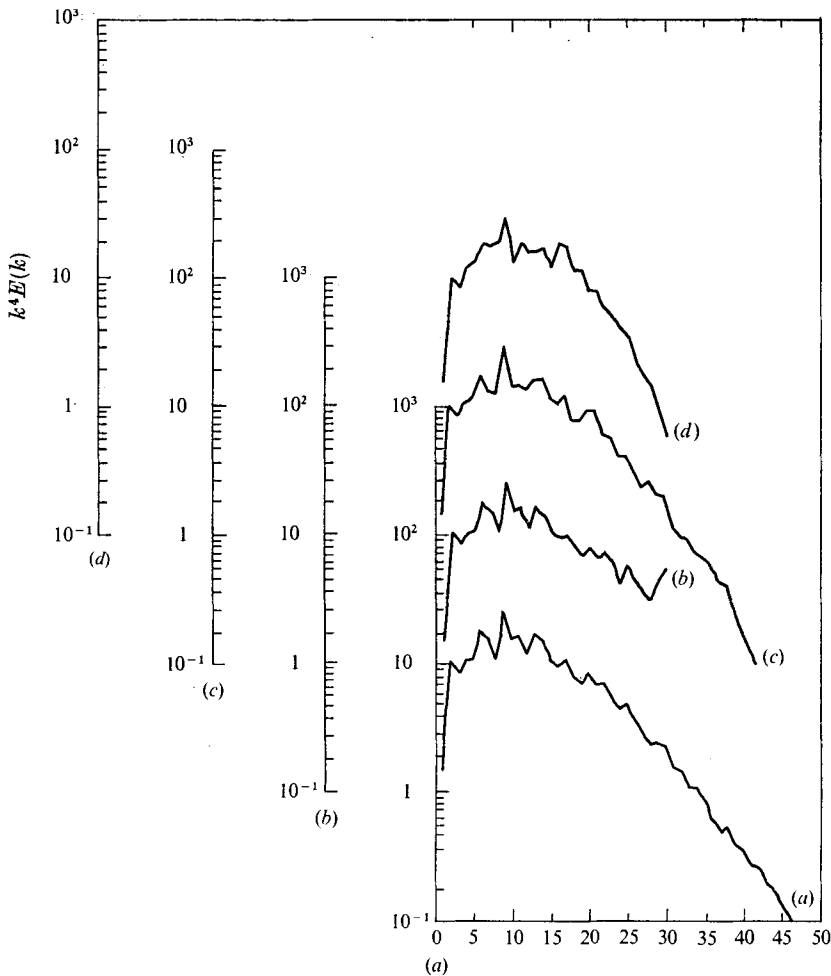
FIGURE 1. Plot of $k^4E(k)$ vs. k at $t = 2$, for computer experiment described in § 3 of text. (a) Spectral method with $(128)^2$ independent wavenumbers (called $S128$) and cut-off wavenumber $k_c = 63$. (b) Spectral method with $(64)^2$ wavenumbers (called $S64$) and $k_c = 31$. (c) Arakawa difference scheme with $(128)^2$ grid points (called $F128$). (d) Arakawa difference scheme with $(64)^2$ points (called $F64$). Initial energy spectrum is given by (3.3), $\nu = 0.005$ and initial integral-scale Reynolds number $R_L(0) = 138$.

spectral cut-off k_{max} of $S128$ and $F128$ is $k_{max} = 63$ and, for $S64$ and $F64$, $k_{max} = 31$. For technical details, see Orszag (1971).

In figure 1, we show plots of the enstrophy dissipation spectra $k^4E(k)$ vs. k for the runs with $\nu = 0.005$ at $t = 2$, which is well into the evolution of this flow. We consider the enstrophy dissipation spectrum because, as argued in § 2, it is *the* critical spectrum that determines whether all dynamically important scales are resolved. In order to simulate properly the nonlinear dynamics of two-dimensional turbulence, *it is necessary to resolve all scales of motion that make appreciable contributions to the enstrophy dissipation rate η.* The analogous condition in three dimensions is the resolution of all scales that contribute to the energy dissipation rate (enstrophy). In the limiting case where $\nu \to 0$ but the spatial resolution

remains fixed, η cannot be properly resolved; in this case, the simulation is that of the approach of a conservative dynamical system to statistical mechanical equilibrium, as shown by Fox & Orszag (1973b). In order to be assured *a priori* that a numerical simulation is more faithful to real turbulence than to one of the latter inviscid equipartition states, it is necessary to demand adequate spectral resolution of η.

Returning to the results plotted in figure 1, we see that all four runs have adequate resolution for this case, according to the criterion that all scales that can contribute appreciably to

$$\int_0^\infty k^4 E(k)\, dk$$

be resolved. However, the differences between the four spectra are noteworthy. In the spectral range $1 \leqslant k \leqslant 25$, $S64$ and $S128$ are virtually identical. Differences in the details of the flows obtained spectrally by $S64$ and $S128$ are evident on considering the vorticity contours shown in figure 2. The only discrepancies between $S128$ (figure $2a$) and $S64$ (figure $2b$) are in the very smallest scales. The truncation from 128×128 modes to 64×64 modes has done nothing more than affect the flow in the scales in the immediate vicinity of the spectral cut-off.

Comparison of $F128$ (figure $1c$) with $S128$ (figure $1a$) shows spectral differences that are numerically evident for $k > 5$; the qualitative features of the spectrum are changed for $k > 10$. The spectral results for $F64$ shown in figure $1(d)$ suggest numerical inaccuracy for $k > 3$. These results are substantiated by examination of the vorticity contours shown in figure 2. Although figure $2(b)$ is somewhat 'choppy' the location and intensity of flow features on scales larger than about 4 grid intervals are nearly identical to those in figure $2(a)$. The contours of figure $2(c)$ for $F128$ do not follow those of $S128$ as strongly, although the large-scale features and some of the small-scale features bear good qualitative resemblance. The contours of figure $2(d)$ for $F64$ do not follow those of any of the other calculations very closely. Truncation of the finite-difference calculation from 128×128 to 64×64 grid points has a significant effect on the results. Notice that it would be difficult to predict *a priori* that $F64$ has significant errors in the vorticity since the spectrum $k^2 E(k)$ of vorticity tapers off to zero as k increases even more rapidly than the enstrophy dissipation spectrum shown in figure $1(d)$. One of the most important conclusions from the accuracy comparisons of the present section is that the spectral results *signal* their accuracy or inaccuracy through an inadequately resolved enstrophy dissipation spectrum; on the other hand, finite-difference methods tend to misrepresent high wavenumber interactions so the results may *look* reasonable even when they are significantly in error.

The stream function at $t = 2$ with $\nu = 0.005$ is contoured in figure 3 using the results of $S128$. Since the stream function is dominated by the largest scales of motion, the differences between $S64$, $S128$, $F64$ and $F128$ are quite small. The result illustrates another of our points: notions of accuracy depend strongly on what is being measured. $F64$ is quite adequate for obtaining accurate contours of the stream function, but it is not adequate for vorticity contours.

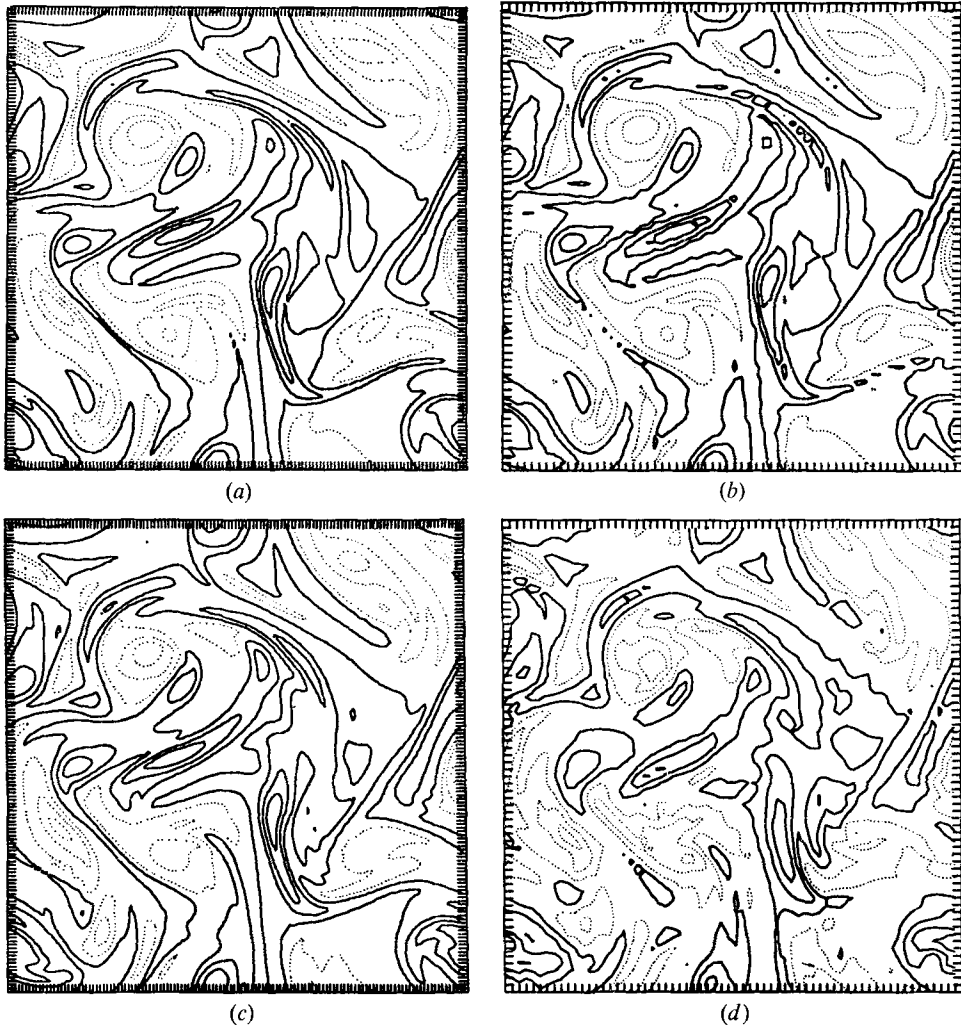Two major points have been illustrated by the comparison of runs with

FIGURE 2. Vorticity contours for (a) $S128$, (b) $S64$, (c) $F128$ and (d) $F64$ at $t = 2$. Nomenclature is explained in caption to figure 1. Initial energy spectrum is (3.3), $\nu = 0.005$ and $R_L(0) = 138$.

$\nu = 0.005$. First, spectral calculations are roughly equivalent in accuracy to finite-difference calculations with *twice* the resolution in each space direction. Second, the spectral results signal their accuracy and inaccuracy while the finite-difference results conspire to hide such inaccuracy. The first of these points is further illustrated by the results plotted in figure 4, which shows the enstrophy dissipation rate as a function of time for $S128$, $S64$, $F128$ and $F64$ when $\nu = 0.0025$. Besides illustrating the similar accuracy of $S64$ and $F128$ for this case, figure 4 shows that $t = 2$ is well into the evolution of these flows and that nonlinear interaction acts strongly to enhance the value of η. (In the absence of nonlinear interaction η is monotonically decreasing as t increases.)

The runs with $\nu = 0.0025$ and $\nu = 0.001$ illustrate these same two points even
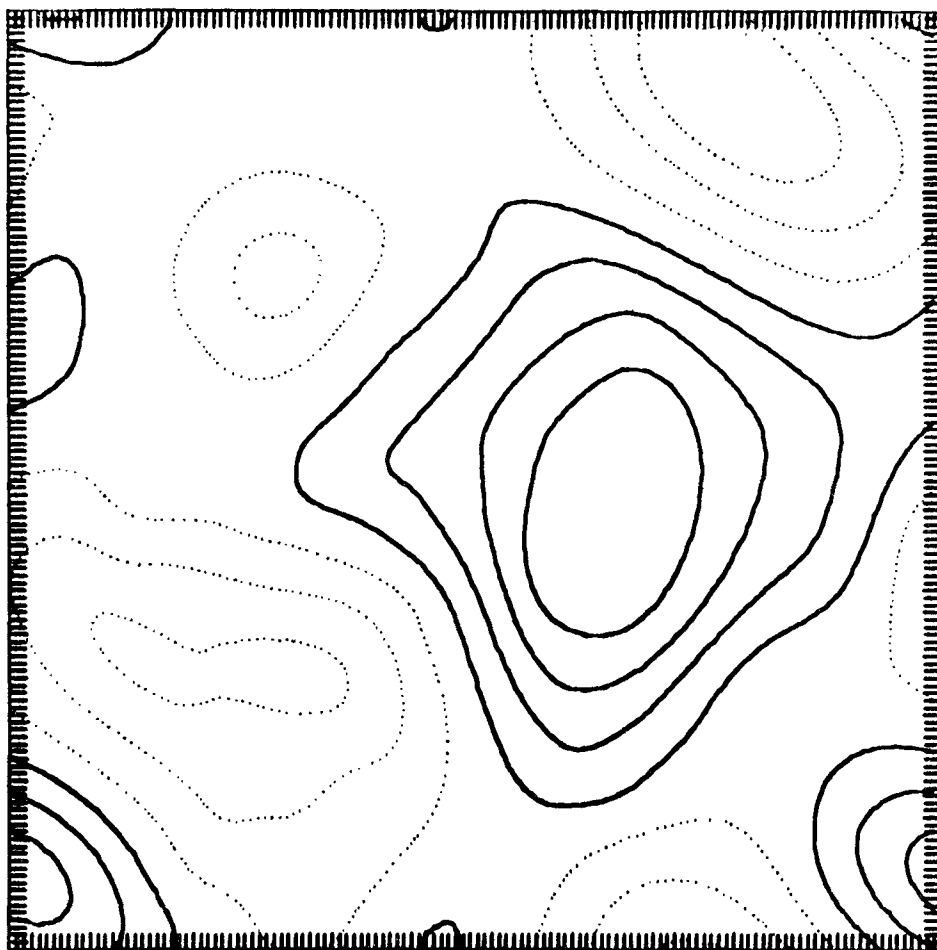
FIGURE 3. Stream-function contours for run $S128$ at $t = 2$. Initial energy is (3.3), $\nu = 0 \cdot 005$ and $R_L(0) = 138$. Nomenclature as in caption to figure 1.

more dramatically. The enstrophy dissipation spectra for $\nu = 0 \cdot 0025$ are shown in figure 5. The analysis of these spectra follows closely the discussion given above for $\nu = 0 \cdot 005$. Comparison of figure 5 (a) with figure 5 (b) shows the remarkable result that, even though the enstrophy dissipation spectrum of $S128$ is beginning to show signs of a build-up in the highest wavenumber (and, hence, inadequate resolution of η), the enstrophy dissipation spectra of $S64$ and $S128$ are nearly identical for $k \leqslant 14$. Similarly, $F128$ is trustworthy only for $k \leqslant 7$, while $F64$ is accurate only for $k \leqslant 3$. The vorticity contours at $t = 2$ with $\nu = 0 \cdot 0025$ are shown in figure 6. Although the enstrophy dissipation spectrum for $S64$ is rather poorly behaved near the cut-off, the prominent features of the vorticity contours for $S64$ reproduce rather well those of $S128$ in both location and intensity. On the other hand, the contours of $F128$ are smooth and apparently well behaved, but they are in fact not very accurate; the enstrophy dissipation spectrum of $F64$ does not signal disaster because it tapers off nicely as k increases, but in fact the contours of vorticity are quite inaccurate.
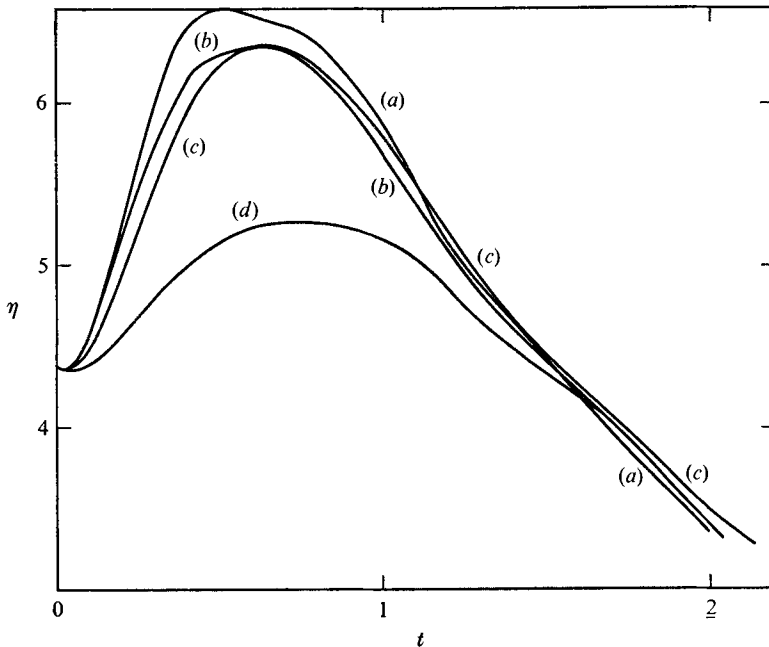
FIGURE 4. Enstrophy dissipation rate $\eta(t)$ as a function of time for the four runs (a) $S128$, (b) $S64$, (c) $F128$ and (d) $F64$. Nomenclature as in caption to figure 1. Initial energy is (3.3), $\nu = 0.0025$ and $R_L(0) = 349$.

Enstrophy dissipation spectra for $t = 2$, $\nu = 0.001$ are presented in figure 7, while the corresponding vorticity contours are given in figure 8. Apparently, the enstrophy dissipation spectrum of $S64$ is accurate only for $k \leqslant 13$, while that of $F128$ is accurate only for $k \leqslant 7$. The similarity of the spectrum of figure 7 (a) with that of figure 5 (b) suggests that the enstrophy dissipation spectrum of $S128$ is accurate for $k \lesssim 25$, but this is a dangerous conclusion. These runs with $\nu = 0.001$ are clearly at the limits of the ability of the present simulations to produce accurate results.

The integral-scale Reynolds number R_L for the run with $\nu = 0.005$ is approximately 138 at $t = 0$; with $\nu = 0.0025$, $R_L \simeq 349$, while with $\nu = 0.001$, $R_L \simeq 1184$. At $t = 2$, the corresponding Reynolds numbers R_L are 146, 345 and 900, respectively. We conclude that $F64$ is moderately accurate for $R_L \lesssim 150$, $F128$ and $S64$ are moderately accurate for $R_L \lesssim 350$, and $S128$ is moderately accurate for $R_L \lesssim 1100$. On the other hand, Lilly (1971) used a scheme very similar to $F64$ to calculate two-dimensional turbulence at $R_L = 315$, 411 and 537. The spectra he obtained are similar to those given by $F64$ at the higher Reynolds numbers. This suggests that Lilly's simulations may not be accurate and that the rapidly falling dissipative tail he found in the spectra produced by the finite-difference scheme is a false indication of accuracy. Deem & Zabusky (1971) used a scheme similar to that of $F128$ to obtain results at $R_L \approx 2200$. Again, we conclude that their simulation is unreliable at the small scales where they sought to identify properties of the inertial range.
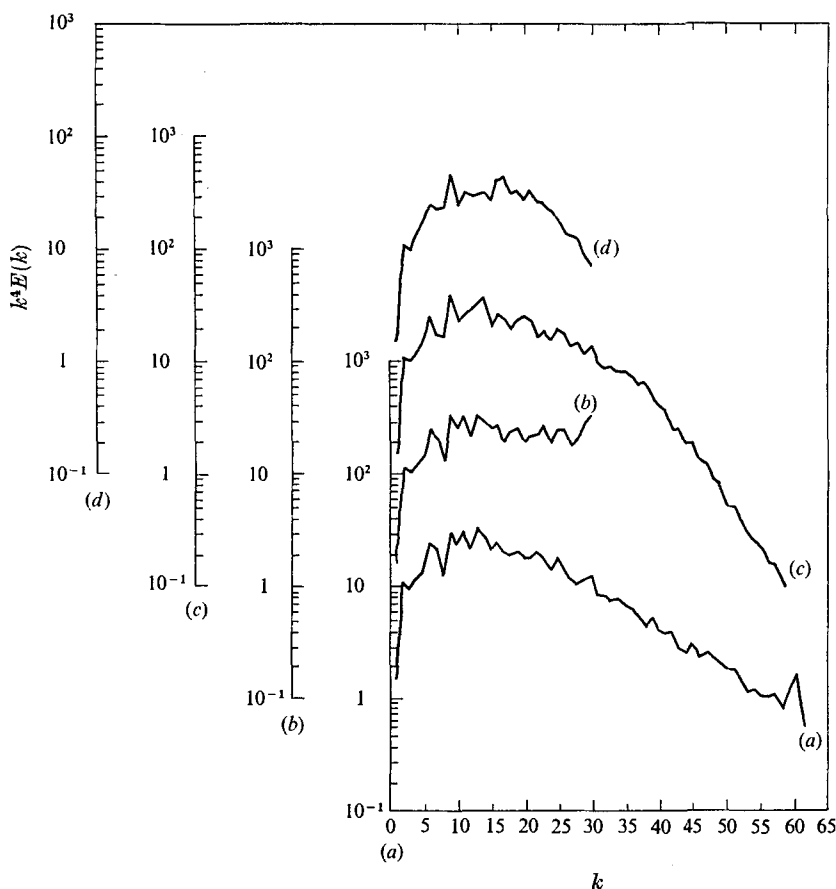
FIGURE 5. Plot of $k^4 E(k)$ *vs.* k for (a) $S128$, (b) $S64$, (c) $F128$ and (d) $F64$ at $t = 2$. Nomenclature as in caption to figure 1. Initial energy spectrum is (3.3), $\nu = 0.0025$ and $R_L(0) = 349$.

4. High Reynolds number numerical simulations

In this section, we address two questions. First, can the inertial range of two-dimensional turbulence be studied with the present simulations? If not, what is a reasonable estimate of the resolution that will be required? Second, what are the prospects for the numerical simulation of very high Reynolds number turbulence in general?

The answer to the first question is definitely no. By definition, the enstrophy inertial range must contain a wavenumber below which lies most of the enstrophy of the flow and above which lies most of the enstrophy dissipation. If the energy spectrum obeys a power law in the inertial range then the power-law exponent must lie between -5 and -3 by these requirements. Thus, the enstrophy dissipation spectrum $k^4 E(k)$ has a power-law exponent between -1 and 1 in the inertial range. Now if we refer back to the simulations reported in §3, we concluded that $S128$ was but marginally accurate for all k when $\nu = 0.0025$. However, it is evident from figure 5 (a) that most enstrophy dissipation occurs for $k < 20$, so the inertial range must be confined to $k \leqslant 20$; it is clear that there are scant data
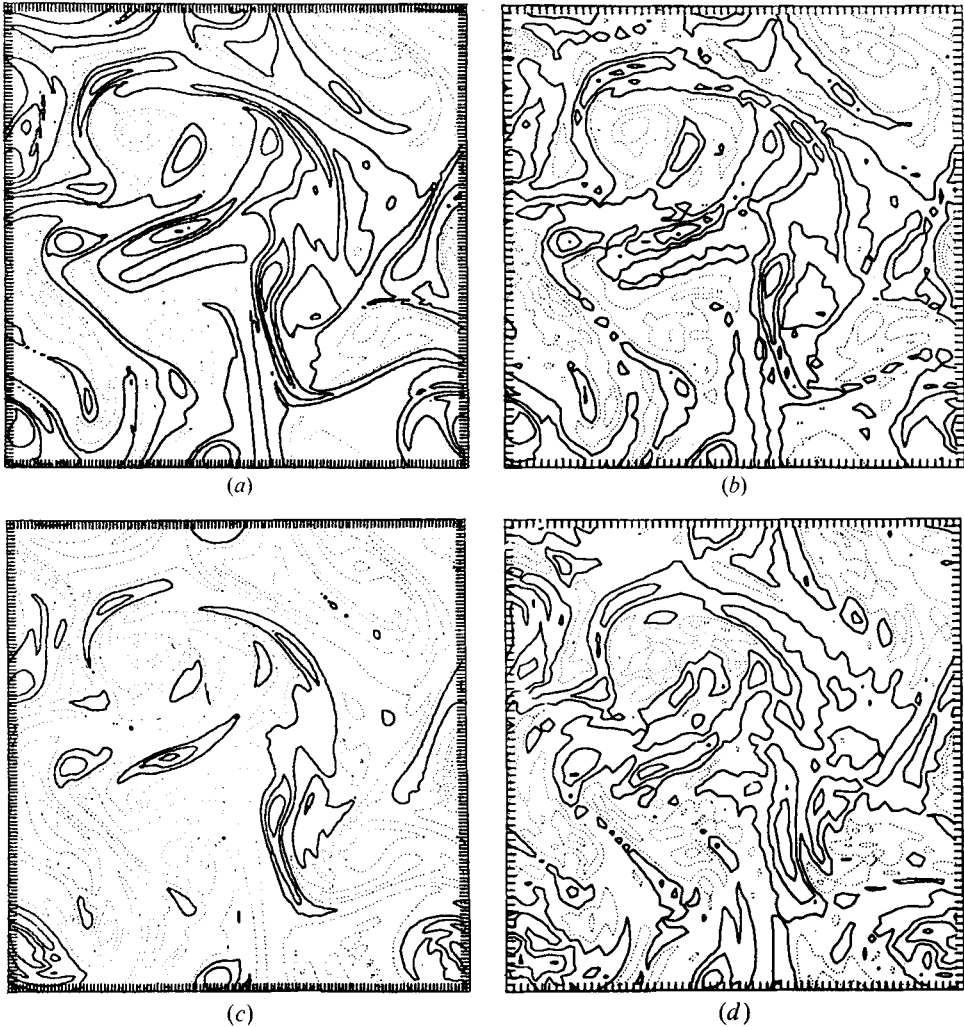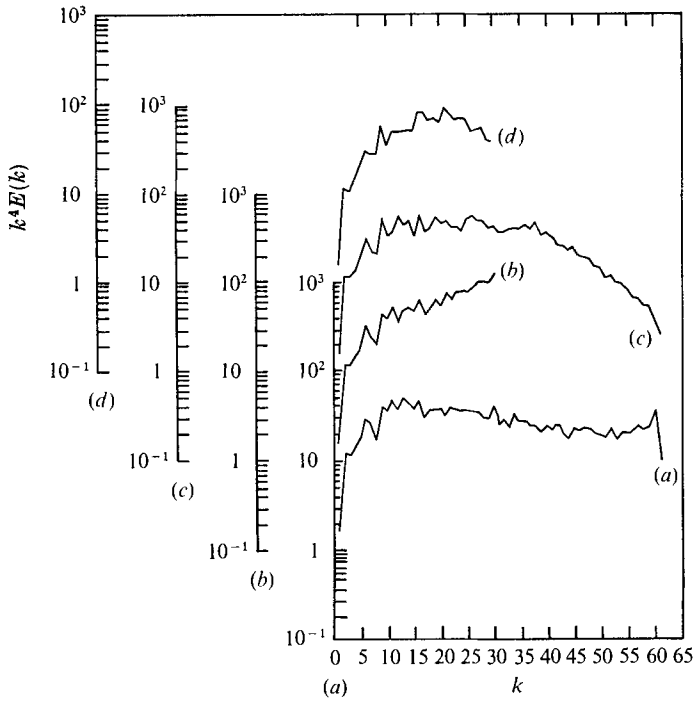
FIGURE 6. Vorticity contours for (a) $S128$, (b) $S64$, (c) $F128$ and (d) $F64$ at $t = 2$. Nomenclature as in caption to figure 1. Initial energy spectrum is (3.3), $\nu = 0\cdot0025$ and $R_L(0) = 349$.

to verify *any* inertial-range power law for $S128$ with $\nu = 0\cdot0025$. We conclude that the present simulations cannot determine the correctness of theories of asymptotic two-dimensional inertial ranges.

It was also inferred in § 3 that $S128$ with $\nu = 0\cdot001$ is possibly accurate for $k \lesssim 25$, but certainly not beyond. The spectrum shown in figure 7 (a) has a substantial region where $E(k) \sim k^{-4}$ for $k \lesssim 25$. But, emphatically, we cannot conclude that the asymptotic inertial-range spectrum is k^{-4}. Figure 9 compares the enstrophy dissipation spectrum depicted in figure 7 (a) with the ($\lambda = 1$) test-field model discussed in §§ 6 and 7. The initial conditions, viscosity and time of evolution for these curves match those for the simulations. The solid line has the same upper and lower wavenumber truncation as the $S128$ simulation, while the dashed line has an upper wavenumber truncation of $k_{max} = 128$. (The effect of

FIGURE 7. Plot of $k^4E(k)$ *vs.* k for (a) $S128$, (b) $S64$, (c) $F128$ and (d) $F64$ at $t = 2$. Nomenclature as in caption to figure 1. Initial energy spectrum is (3.3), $\nu = 0.001$ and $R_L(0) = 1184$.
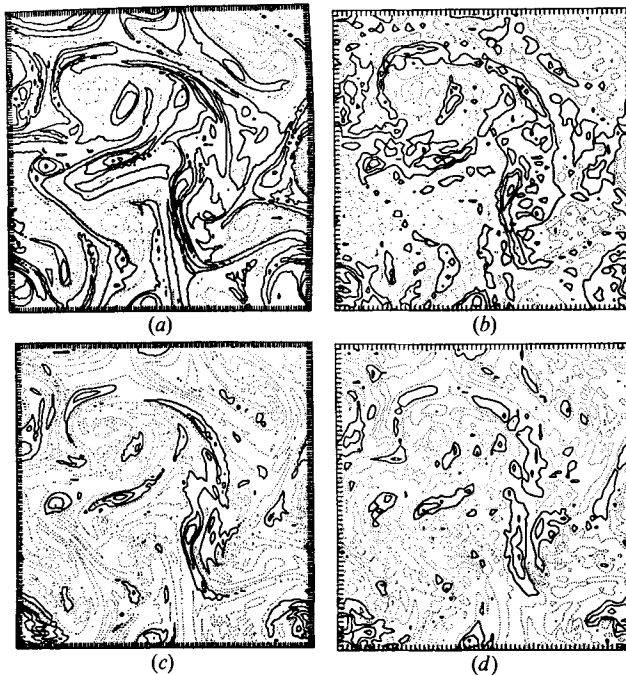

FIGURE 8. Vorticity contours for (a) $S128$, (b) $S64$, (c) $F128$ and (d) $F64$ at $t = 2$. Nomenclature as in caption to figure 1. Initial energy is (3.3), $\nu = 0.001$ and $R_L(0) = 1184$.
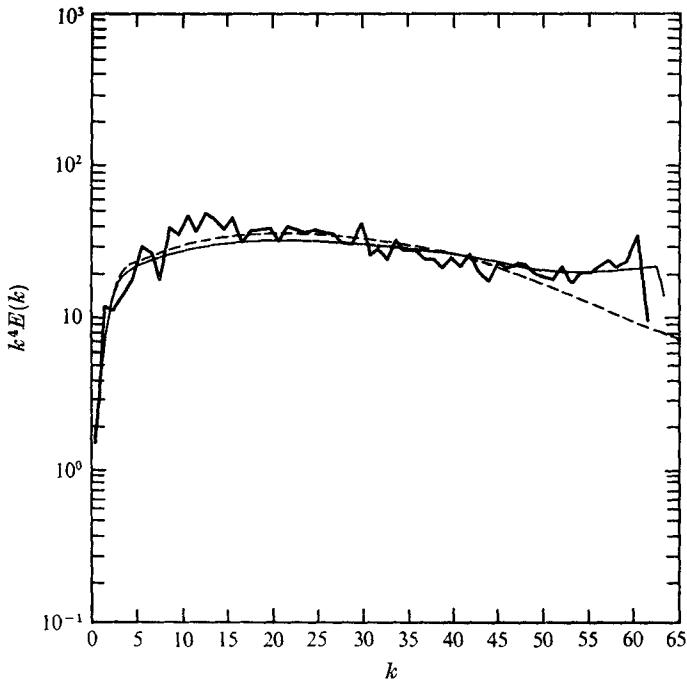
FIGURE 9. Comparison of $k^4 E(k)$ vs. k. ——, run $S128$; ——, test-field model with $k_{max} = 63$ (the same cut-off as $S128$); ----, test-field model with $k_{max} = 128$.

the wavenumber cut-off for the latter curve is negligible, since $k^4 E(k)$ at $k = 128$ has decreased by four orders of magnitude from its peak value.) Comparing the numerical experiment with the equivalent result of the test-field model, we see that there is close agreement over the entire spectrum range and, in particular, the curve from the test-field model reproduces the -4 region of the spectrum. However, the asymptotic inertial-range spectrum for the test-field model goes not like k^{-4} but like k^{-3} with a logarithmic correction (Leith & Kraichnan 1972). The present results differ from asymptotic form for at least three reasons: the finite high wavenumber truncation, depression of the high wavenumber spectrum by dissipation, and the non-localness for the dynamical interaction in wavenumber (Kraichnan 1971 b).

It is apparent from the comparisons of § 3 that the simulations with $\nu = 0.001$ would be marginally accurate at all scales with 256×256 spectral resolution; a simulation with 512×512 resolution might possibly permit observation of an inertial range. The calculations with a 512×512 spectral code are now underway.

The second question posed at the beginning of this section concerned more generally the prospects for simulations of very high Reynolds number turbulence. It may be shown from (2.13) that as R_L increases the required spectral resolution grows like $R_L^{\frac{1}{2}}$; the total number of modes must grow like R_L. Also, it may be shown that the number of time steps required for the flow to evolve significantly grows like $R_L^{\frac{1}{2}}$; consequently, the total work in each simulation grows like $R_L^{\frac{3}{2}}$. If computers improve in efficiency by a factor of 1000, the maximum Reynolds number that can be simulated increases by a factor of about 100. Clearly,

extrapolation of these estimates to Reynolds numbers like those of the atmosphere suggests that direct numerical simulation is not economical by the present method.

On the other hand, the results presented in § 3 provide an intriguing possibility for avoiding the computing-time dilemma just encountered. Comparison of the contours of figures 2(a), 6(a) and 8(a) shows some remarkable resemblances. Apart from additional small eddy structures introduced as the Reynolds number increases, all three simulations using $S128$ are virtually identical. In other words, despite the variation of R_L over a range of 7·5 from $\nu = 0.005$ to $\nu = 0.001$, the large-scale features of the flows are nearly identical; there is strong Reynolds number independence of the large-scale features of the flows. Examination of the enstrophy dissipation spectra in figures 1(a), 5(a) and 7(a) shows appreciable structural differences only for $k > 10$, so that we infer that wavenumbers $k \leqslant 10$ are approximately Reynolds number independent over the range $R_L = 150-1100$.

In summary, the suggestion that is being made is that it is not necessary to simulate high Reynolds number turbulence at high Reynolds number if one is only interested in wavenumbers $k < k^*$, say. Rather, we suggest that it is only necessary to simulate a flow whose enstrophy dissipation spectrum peaks at a wavenumber somewhat larger than k^*, even though the Reynolds number of the latter flow may be several orders of magnitude less than that for the flow of interest. The wavenumbers $k < k^*$ should be Reynolds number independent. Clearly, this idea should be subjected to much closer scrutiny in the future.

5. Formulation of statistical theory of two-dimensional turbulence

The statistical theory of two-dimensional turbulence has been discussed in some detail by Kraichnan (1967) and Leith (1971). We refer the reader to these papers for a discussion of the physical mechanisms of energy transfer, and how it differs from three-dimensional turbulence. Our discussion here is confined to a brief statement of the equations of motion for the velocity covariances, according to the direct-interaction approximation and test-field model.

We are interested here in determining the covariance

$$U_{ij}(\mathbf{k}, t, t') = (D/2\pi)^2 \langle u_i(\mathbf{k}, t) u_j(-\mathbf{k}, t') \rangle = (\delta_{ij} - k_i k_j / k^2) U(k, t, t'). \quad (5.1)$$

The second equality in (5.1) follows from isotropy with $U(k, t, t')$ given by (2.3). The equation in the direct-interaction approximation for the modal covariance U is (Kraichnan 1959)

$$(\partial/\partial t + \nu k^2) U(k, t, t') = S(k, t, t'), \quad (5.2)$$

where

$$S(k, t, t') = \int_\Delta dp\, dq\, A(k, p, q) \int_0^{t'} g(k, t', s)\, U(k, t, s)\, U(p, t, s)\, ds$$
$$- \int_\Delta dp\, dq\, B(k, p, q) \int_0^t U(k, t', s)\, g(p, t, s)\, U(q, t, s)\, ds. \quad (5.3)$$

In (5.3)
$$A(k, p, q) = \tfrac{1}{2}(B(k, p, q) + B(k, q, p)) \quad (5.4)$$

and, for two dimensions (Leith 1971),

$$B(k, p, q) = (2/k^2)(k^2 - q^2)(p^2 - q^2)(1 - x^2)^{\frac{1}{2}}. \quad (5.5)$$

The symbol $\displaystyle\int_\Delta$ in the above equations indicates integration over all $\mathbf{p}$ and $\mathbf{q}$ such that $\mathbf{k}$, $\mathbf{p}$ and $\mathbf{q}$ form a triangle, while x, y and z designate the cosines of the interior angles opposite the sides $\mathbf{k}$, $\mathbf{p}$ and $\mathbf{q}$ respectively. In (5.3) there also appears the modal decorrelation or Green's function $g(k, t, t')$ which describes relaxation of the modal intensity $U(k, t, t')$ under the joint action of turbulence and viscosity. Its equation is

$$(\partial/\partial t + \nu k^2)\, g(k, t, t') = -\int_\Delta dp\, dq\, B(k, p, q) \int_{t'}^{t} g(k, s, t')\, g(p, t, s)\, U(q, t, s)\, ds, \quad (5.6)$$

with
$$g(k, t', t') = 1.$$

The equation for the energy spectrum $E(k, t) = \pi k U(k, t, t)$ follows from (5.2) and (5.3) by forming the equation for $\partial U(k, t', t)/\partial t'$, adding the result to (5.2) and taking the limit $t = t'$. The result is (2.4), with

$$T(k, t) \equiv 2\pi k S(k, t, t). \quad (5.7)$$

We note that energy and enstrophy conservation as stated by (2.6) may be directly established from the structure of $S(k, t, t)$, as given by (5.3).

The test-field model may best be described, formally, as an abridgement and alteration of the direct-interaction approximation. The changes are as follows. First, retain (5.2) and (5.3) only for $t = t'$. To evaluate the $U(k, t, s)$ terms that occur on the right-hand side of (5.3) use the prescription

$$U(k, t, s) = U(k, t, t)\, g(k, t, s) \quad (t \geqslant s). \quad (5.8)$$

Next, replace the g equation (5.6) by

$$(\partial/\partial t + \nu k^2)\, g(k, t, t')$$
$$= -\lambda^2 \int_\Delta dp\, dq\, B^{\mathrm{TFM}}(k, p, q)\, g(k, t, t') \int_0^t ds\, g(k, t, s)\, g(p, t, s)\, g(q, t, s)\, U(q, t, t), \quad (5.9)$$

where
$$B^{\mathrm{TFM}}(k, p, q) = (1 - x^2)^{-\frac{1}{2}} (1 - y^2)(1 - z^2)\, k^2.$$

Here, λ is a parameter whose value is yet to be fixed. The result of the above changes is that the integral equations for U and G may be replaced by an equivalent set of ordinary differential equations, which greatly speeds up numerical computations as compared with those for the direct-interaction approximation, at least for homogeneous flows. Moreover, these alterations produce a theory for which $U(k, t, t)$ is properly invariant to random Galilean transformations, thereby leading to a theory which has a proper qualitative inertial-range structure. For motivations, rationale and further details see Kraichnan (1971a) and Leith & Kraichnan (1972).

We note that the direct-interaction approximation is a complete, deductive approximation. No empirical constants enter (5.2) or (5.3) for the determination of U and from initial conditions $U(k, 0, 0)$. This is not true for the test-field model because of the parameter λ entering (5.9). The choice $\lambda = 1$ appears most natural in terms of the theoretical foundations of the model. However, this choice does not emerge uniquely from the theoretical analysis, and in the present paper we examine sensitivity to changes in λ.

6. Comparison of computer simulations with theories

Results for energy and transfer spectra

Two initial energy spectra $E(k, 0)$ are chosen to compare the theories with computer experiments. Spectrum I is

$$E(k, 0) = 16(2/\pi)^{\frac{1}{2}} v_0^2 (k/k_0)^4 k_0^{-1} \exp\left(-2(k/k_0)^2\right) \tag{6.1}$$

and spectrum II is given by (3.3).

Values of the various integral length scales and Reynolds numbers defined in §2, as well as v_0 and k_0, are listed in table 1. Also given are values of the kinematic viscosity ν, lower wavenumber cut-off k_{low} and the upper wavenumber cut-off k_{up}. All nonlinear interactions which involve any wavenumber outside the range $(k_{\text{low}}, k_{\text{up}})$ are discarded. Contributions to any spectral integral are likewise discarded exterior to this range.

	v_0	k_0	k_{low}	k_{up}	ν	R_l	l^{-1}	R_L	L^{-1}
I	1·0	8·0	1·0	63·0	0·0050	19·56	10·59	58·6	4·18
II	1·0	$\frac{3}{2}$	1·0	63·0	0·0025	20·0	9·49	361·92	1·35

TABLE 1

Case I has low R_L and moderate R_l, whereas case II has high R_L and moderate R_l. We also note that according to (6.1) there is initially very little energy for $k < k_0$, and $k_0 = 8k_{\text{low}}$, so that for case I there could be appreciable back transfer to low wavenumbers. For case II, $k_0 = \frac{3}{2}k_{\text{low}}$, so that in this case only a small range of wavenumbers is available for back transfer.

Case I is used to assess the accuracy of the theories in treating back transfer to smaller wavenumbers, whereas case II is primarily used to study enstrophy cascade to large wavenumbers. As we shall shortly see, both cases exhibit rather strong nonlinear transfer. Simulation runs with smaller viscosities, but conditions otherwise the same as in cases I and II, begin to show perceptible truncation errors in the enstrophy dissipation spectrum at large k.

Our procedure in comparing theory and numerical simulation is to first examine the time dependence of the integral quantities described in §4. We then examine the spectra of $E(k, t)$, $D(k, t)$ and $T(k, t)$ at some dynamically significant time into the decay $(t = 0·8)$.

Figures 10–13 give $\Omega(t)/\Omega(0)$, $\pi_B(t)/D(0)$, $\eta(t)/\eta(0)$, $\pi_F(t)/\eta(0)$, $S_2(t)$ and $R_L(t)/R_L(0)$ for case I. Figures 14–17 give the same integral quantities for case II. They are defined in (2.7), (2.8), (2.14), (2.16) and (2.17). Initial values for these quantities are given in the figure captions. The figures compare two computer experiments (given by the points and the crosses) with the direct-interaction approximation (dotted lines) and the test-field model (with $\lambda = 0·65$, solid lines, and $\lambda = 1$, dot–dashed lines). The points enclosed in a circle or square shown in figures 10, 12 and 13 represent values averaged over the two realizations, whereas the points and crosses are unaveraged computer-simulated values. The two computer simulations differ only in the particular Gaussian realization for the initial
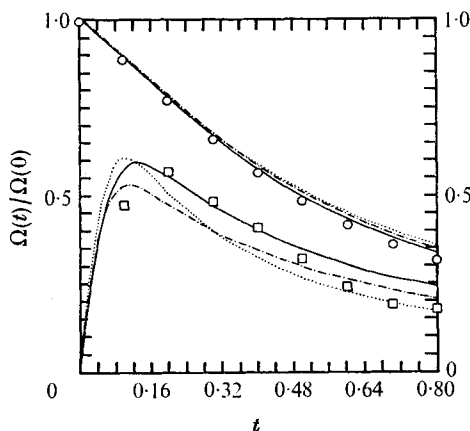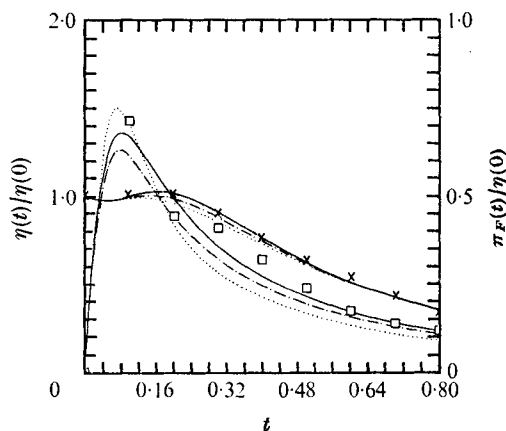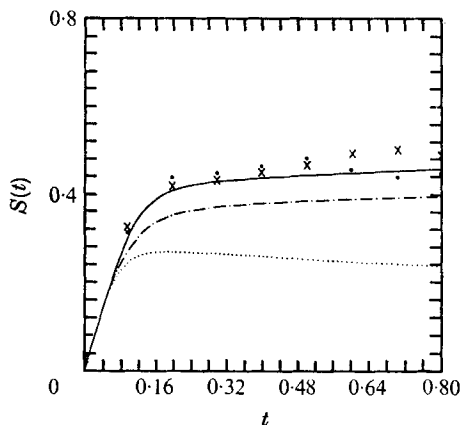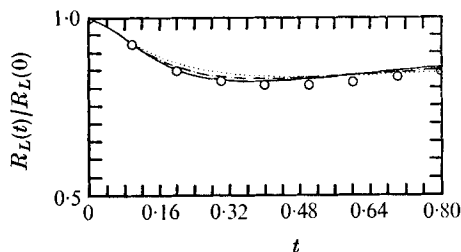
FIGURE 10

FIGURE 11

FIGURE 12

FIGURE 13

FIGURE 10. Enstrophy $\Omega(t)$ [see (2.8)] and total energy back-transfer function $\pi_B(t)$ [see (2.16)] as functions of time. $\Omega(t)$ is normalized by $\Omega(0)$ and $\pi_B(t)$ by $D(0)$. ——, test-field model, $\lambda = 0.65$; —·—, test-field model, $\lambda = 1$; ..., direct-interaction approximation; O, computer-experiment values of $D(t)$ averaged over two realizations; □, similarly averaged values of $\pi_B(t)$. Initial energy spectrum is (6.1). Further parameters of run are given in table 1, case I.

FIGURE 11. Enstrophy dissipation $\eta(t)$ and total enstrophy forward-transfer $\pi_F(t)$ [see (2.17)] as functions of time. Figure is normalized by $\eta(0)$. Curves show three theories as in figure 10. ×, $\eta(t)$ for a computer experiment; □, averaged computer-experiment values of $\pi_F(t)$ for two numerical realizations of case I. Initial energy spectrum is (6.1). Further parameters of run are given in table 1, case I.

FIGURE 12. Two-dimensional skewness factor $S_2(t)$ [see (2.15)] as a function of time for the three theories (curves, as in figure 10) and two computer experiments (points and crosses). Runs are for case I, whose initial energy spectrum is (6.1). For further details, see table 1.

FIGURE 13. Integral-scale Reynolds number $R_L(t)/R_L(0)$ [see(2.9)] as a function of time for case I. Curves depict the three theories as in figure 10. O, averaged computer-experiment values.
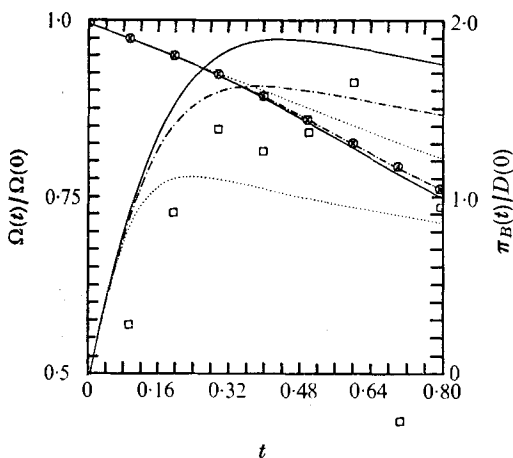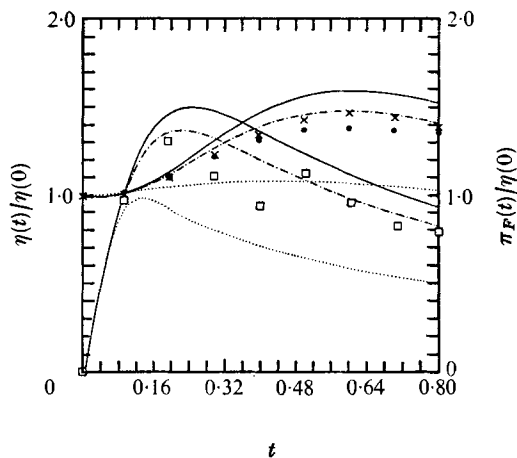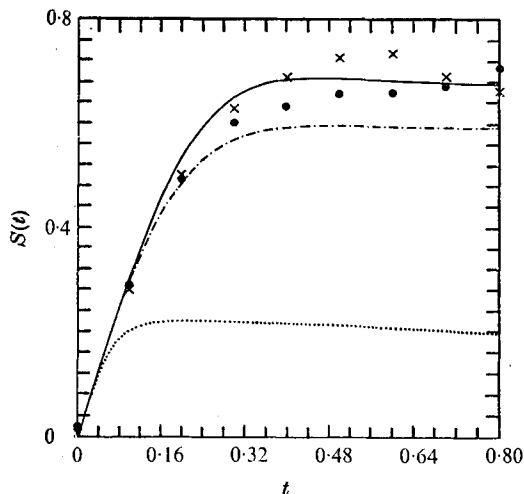
FIGURE 14
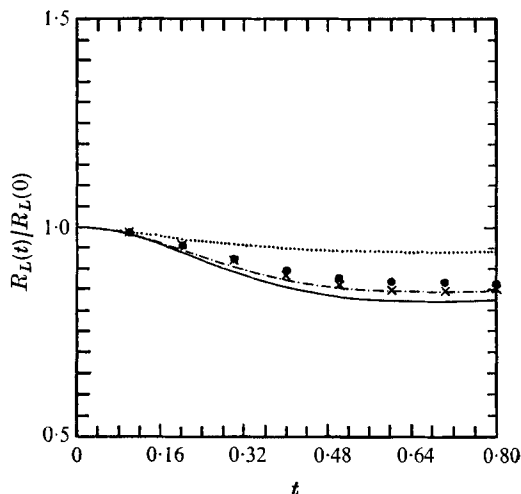

FIGURE 15

FIGURE 16

FIGURE 17

FIGURE 14. Enstrophy $\Omega(t)$ [see (2.8)] and total energy back-transfer function $\pi_B(t)$ [see (2.16)] as functions of time. $\Omega(t)$ is normalized by $\Omega(0)$ and $\pi_B(t)$ by $D(0)$. Curves show three theories as in figure 10. ⊗, computer-experiment values of $D(t)$ averaged over two realizations; □, similarly averaged values of $\pi_B(t)$. Initial energy spectrum is (3.3). Further parameters of run are given in table 1, case II. Note change of scale for $\pi_B(t)$.

FIGURE 15. Enstrophy dissipation $\eta(t)$ and total enstrophy forward-transfer $\pi_F(t)$ [see (2.17)] as functions of time. Figure is normalized by $\eta(0)$. Curves show three theories as in figure 10; ×, ●, $\eta(t)$ for two realizations of computer experiments; □, averaged computer-experiment values of $\pi_F(t)$. Initial energy spectrum is (3.3). Further details of run are given in table 1, case II.

FIGURE 16. Two-dimensional skewness factor $S_2(t)$ [see (2.15)] as a function of time for the three theories (curves, as in figure 10), and two computer experiments (points and crosses). Runs are for case II, whose initial energy spectrum is (3.3). For further details, see table 1, case II.

FIGURE 17. Integral-scale Reynolds number $R_L(t)/R_L(0)$ [see (2.9)] as a function of time for case II. Curves depict the three theories as in figure 10, ×, ●, values for two computer experiments.

data, i.e. $v(k, 0)$. The scatter in the points shown here is a measure of the statistical errors of the simulations.

Before commenting on the accuracy of the theories and interpreting them relative to the simulations, it is of interest to describe briefly the physical significance of the general shapes of the curves given in these figures. For this purpose we recall that the initial statistical state of the system is multi-variate Gaussian. Hence the measures of transfer $\pi_F(t)$ and $\pi_B(t)$ and the enstrophy skewness $S_2(t)$, shown in figures 10–17, start at zero. The build-up of higher-order statistical correlations is indicated by the rapid increase of S_2 from zero towards a saturation value of 0·4 and 0·6 for case I and II respectively. The fact that $S_2(t)$ levels off implies that the decay at large k becomes self-similar, after a correlation build-up time of about $t \simeq 0·6$ for case I, and $t \simeq 0·4$ for case II. Another transient effect is the 'enstrophy dissipation enhancement' depicted in figures 11 and 15. The bulge in these curves is caused by a surge of energy towards higher wave-numbers, during the early time while the energy transfer function is increasing from zero. This effect is very similar to an equivalent dissipation enhancement for analogous three-dimensional turbulence calculations (Herring *et al.* 1973; Herring & Kraichnan 1972; Orszag & Patterson 1972). The decay of $D(t)$ and the decay of $E(t)$ are monotonic, as they must be, because of inviscid energy and enstrophy conservation. The energy decay for both these cases (for $0 \leqslant t \lesssim 1$) can be accurately predicted from pure viscous decay (though this is not true for the higher moments $D(t)$ and $\eta(t)$).

For both cases I and II, $R_L(t)$ eventually becomes an increasing function of t. This behaviour for two-dimensional turbulence was predicted by Batchelor (1969), who argued that $\eta(t) \sim t^{-3}$, hence $E(t) = A + Bt^{-1}$, for the asymptotic state of decaying two-dimensional turbulence. It follows then that

$$R_L(t) \sim (A + Bt^{-1})\, t.$$

We next discuss the accuracy of the theories, considering first the direct-interaction approximation. The most striking feature of this theory discernible from figures 10–17 is its underestimation of energy transfer to large wavenumbers. This is apparent in figures 12 and 16 for the enstrophy skewness. For the low-R_L case I, the degree of skewness underestimation is about a factor of two, while for the high-R_L case II it is more like a factor of three. The underestimation is discernible to a lesser degree in the other figures although the predictions of the direct-interaction approximation for $E(t)$ are accurate both for case I and case II.

On the other hand, the direct-interaction approximation fares best in the energy-containing region, particularly for case I. This is apparent in figures 10 and 11, in which the gross measures of energy back transfer π_B and enstrophy forward transfer π_F are plotted. We note in figure 10 that the direct-interaction approximation is completely competitive with the test-field model in its prediction of the energy back transfer. Its prediction of the enstrophy transfer for case I is nearly as good as that of the test-field model. At higher Reynolds number, how-ever, this agreement even in the energy-containing region appears to deteriorate as is evident from figures 14 and 15.

For the test-field model, the agreement with numerical simulations is much

better for all these figures, either for $\lambda = 1$ or $\lambda = 0.65$. The choice $\lambda = 0.65$ matches the computer experimental value of $S_2(t)$ for both case I and II slightly better than $\lambda = 1$. On the other hand, $\lambda = 1$ fits the $D(t)$ curve for case II better than $\lambda = 0.65$. The value $\lambda = 0.65$ was originally picked because it best matched the $S_2(t)$ data for case II. The smaller value of λ tends to give a better fit to the large-k data, whereas the larger λ tends to fit the small-k region better.

Figures 18–25 display spectra for $E(k,t)$, $k^4E(k,t)$, $T(k,t)$ and $k^2T(k,t)$ for $t = 0.8$ for cases I and II. Also shown in figures 18, 19, 22, and 23 are the initial spectra for $E(k,0)$ and $E(k,0)k^2$ for comparison. The simulation points shown here are averages of the two separate runs. We consider first the low-R_L results depicted in figures 18–21. It is apparent from the $E(k,0.8)$ spectrum depicted in figure 18 that considerable back transfer has occurred during $0 \leqslant t \leqslant 0.8$. $E(1,t)$ has increased during this time by a factor of 10. Both the direct-interaction approximation and test-field model are in good agreement with the simulations in the back-transfer spectral region $(1 \leqslant k \leqslant 8)$. The direct-interaction approximation appears to be slightly better in this region although rather large statistical scatter in the simulation prevents definite conclusions from being drawn as to which theory is superior. It may be thought that the good agreement between theory and simulation in the back-transfer region is accidental since this is a region of poor statistics for the simulation. This is not really true, however. Energy and enstrophy conservation (2.6) partially enforce the accuracy the simulation possesses at larger k on smaller k. If there is little initial energy at small k, as in case I, then most of the latter energy in these modes is transferred from higher k, where statistics are better. Figures 18 and 19 show the test-field model with $\lambda = 1$ to be in excellent agreement with the numerical simulations over the full range of wavenumbers $(1 \leqslant k \leqslant 63)$. The agreement with the test-field model with $\lambda = 0.65$ is only slightly inferior. On the other hand, the direct-interaction approximation agrees with the simulations for $k < 25$, but begins seriously to underestimate energy transfer for $k > 25$–30.

A parenthetical comment with reference to figure 19 is perhaps appropriate at this point. We note that truncation errors in the simulations begin to manifest themselves at large k at $t \simeq 0.6$, despite the smallness of the initial (and final) R_L. The truncation error appears to increase with time and seriously affect the large-k behaviour of the enstrophy dissipation spectrum for $t \gtrsim 1.2$. Hence, there are difficulties in simulating two-dimensional turbulence even for low R_L.

Transfer spectra $T(k,t)$ and $k^2T(k,t)$ are presented in figures 20 and 21 for case I. The rather large scatter in the computer-experiment data, particularly at low k, is sufficient to prevent us from commenting further on the relative accuracy of the theories for these transfer quantities, except to note that the prediction of the direct-interaction approximation for energy transfer near the maximum (or minimum) transfer is somewhat too small. Note that theories and simulation are in accord in predicting very small energy transfer rates over most of the range of k where the enstrophy dissipation is strong. This qualitative behaviour is in accord with theoretical notions (Kraichnan 1967) for large-R_L turbulence.

The spectra for case II are presented in figures 22–25. The computer-experiment energy spectrum shown in figure 20 is in good agreement with the test-field model
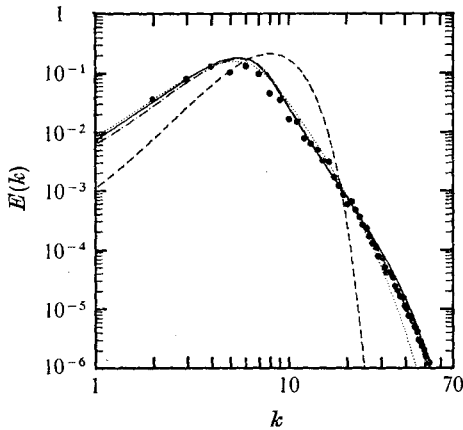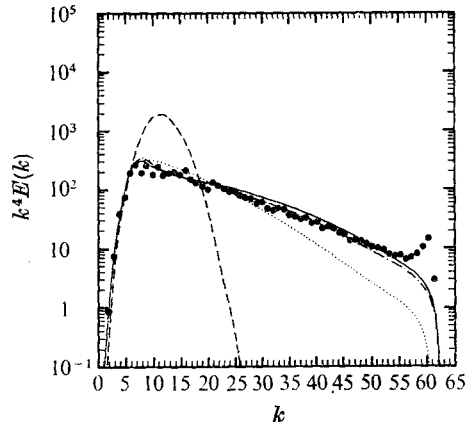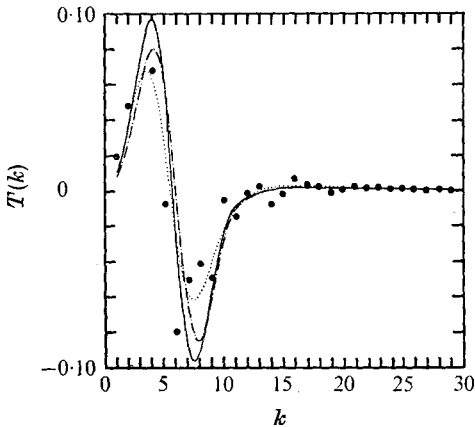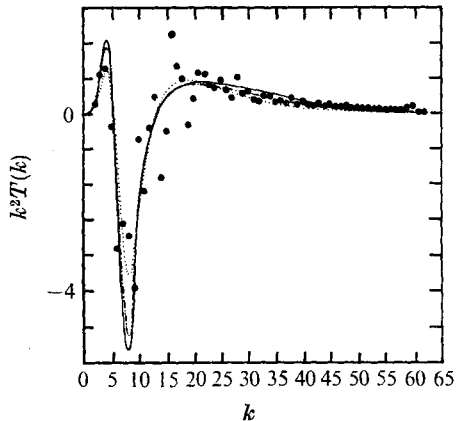
FIGURE 18

FIGURE 19

FIGURE 20

FIGURE 21

FIGURE 18. Comparison of computer-experiment energy spectrum (points) at $t = 0.8$ with the three theories (curves, as in figure 10) for case I (see table 1 for specification of case I). $- - -$, initial theoretical energy spectrum.

FIGURE 19. Comparison of computer-experiment enstrophy dissipation spectrum (points) at $t = 0.8$ with the three theories (curves, as in figure 10) for case I (see table 1 for specification of case I). $- - -$, initial spectrum.

FIGURE 20. Comparison of computer-experiment energy transfer spectrum $T(k)$ (points) with the three theories (curves, as in figure 10) for case I (see table 1). Note change of k-scale as compared with figure 21.

FIGURE 21. Comparison of computer-experiment enstrophy transfer spectrum $k^2 T(k)$ (points) with the three theories (curves, as in figure 10) at $t = 0.8$ for case I (see table 1).

with $\lambda = 1$ over most of the wavenumber range considered. However, we should note that the agreement between theory and computer experiments has deteriorated from that for case I. The theory (for both $\lambda = 1$ and $\lambda = 0.65$) overestimates energy transfer at the highest wavenumbers considered. We again note that the direct-interaction approximation yields satisfactory energy spectra in the
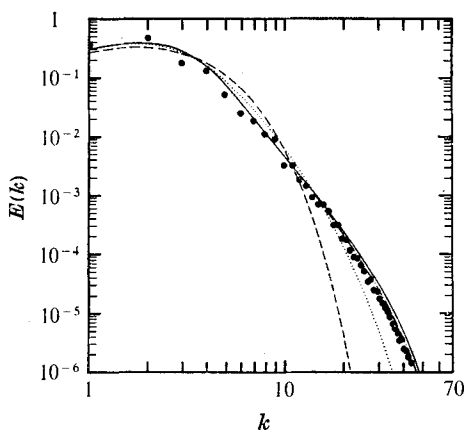
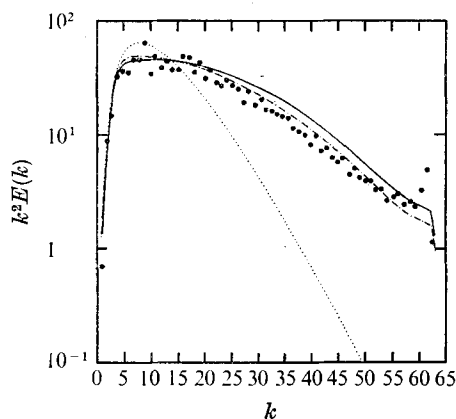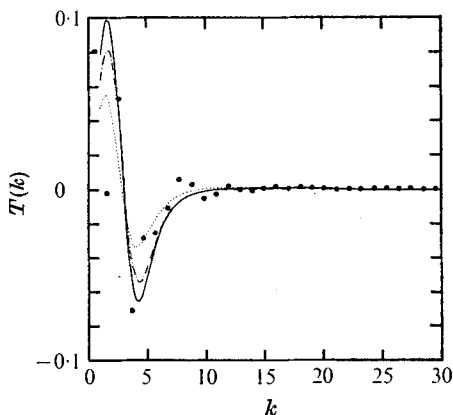FIGURE 22   FIGURE 23
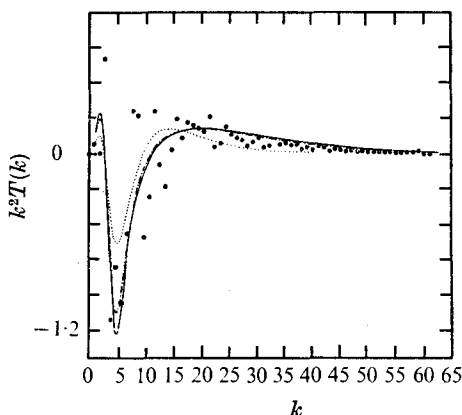

FIGURE 24   FIGURE 25

FIGURE 22. Comparison of computer-experiment energy spectrum (points) with the three theories (curves, as in figure 10) at $t = 0.8$ for case II (see table 1). – – –, initial theoretical energy spectrum.

FIGURE 23. Comparison of computer-experiment enstrophy dissipation spectrum (points) with the three theories (curves, as in figure 10) at $t = 0.8$ for case II (see table 1).

FIGURE 24. Comparison of computer-experiment energy transfer spectrum $T(k)$ [point, see (2.4)] with the three theories (curves, as in figure 10) at $t = 0.8$ for case II (see table 1). Note change of k-scale as compared with figure 21.

FIGURE 25. Comparison of computer-experiment enstrophy transfer spectrum $k^2T(k)$ (points) with the three theories (curves, as in figure 10) at $t = 0.8$ for case II (see table 1).

energy-containing region but poor results in the enstrophy range, according to figure 23. It is of interest to note that neither simulation nor theory gives a k^{-3} range. We have noted elsewhere that this value of R_L is too small to expect such an enstrophy-based inertial range.

The transfer spectra $T(k, 0.8)$ and $k^2T(k, 0.8)$ are shown in figures 24 and 25. As for case I, we note the large scatter in the computer-experiment points. The

test-field model with $\lambda = 1$ again appears to be in satisfactory accord with the computer simulations. In this case, the energy transfer is extremely small, as compared with its value for case I depicted in figure 20, throughout the enstrophy dissipation range.

7. Concluding remarks

The close agreement between the computer simulations and the test-field model suggests that both give good approximations to the spectral evolution of two-dimensional turbulence in the Reynolds number range which has been examined. The wavenumber-range truncation at $k = 64$ appears to cause substantial error only in the tail of the enstrophy dissipation curve at the highest Reynolds numbers treated, and here this error does not appreciably affect the total range of enstrophy dissipation.

The test-field model fits the computer experiments well both for $\lambda = 1$ and $\lambda = 0.65$, and the model does not display much sensitivity to the value of this parameter. The value $\lambda = 1$ works well also in three-dimensional calculations both at high and low Reynolds numbers (Kraichnan 1971b; Herring & Kraichnan 1972). The direct-interaction approximation underestimates enstrophy transfer at high wavenumbers and consequently poorly represents the enstrophy dissipation curves. However, it appears to give an adequate approximation to the back transfer of energy to lower wavenumbers and to the total rate of transfer of enstrophy to higher wavenumbers, with deterioration in the accuracy of the latter quantity showing at the highest Reynolds numbers examined.

The inaccuracy of the direct-interaction approximation for the high wave-number transfer may be traced to a fundamental inadequacy of the approximation in sorting out the dynamical effects of intrinsic distortion of small-scale structures from the effects of simple convection of these structures by the large-scale velocity field (Kraichnan 1964). When both effects are present, the build-up of energy- and enstrophy-transferring triple correlations according to the direct-interaction approximation is limited by the convective decorrelation time rather than the physically relevant, and longer, characteristic time for internal distortion. This may be described formally as a lack of invariance of the transfer to random Galilean transformation (Kraichnan 1964). The effect is more severe in two dimensions than in three because the asymptotic spectrum in the enstrophy-transferring inertial range falls off more steeply, so that there is a greater difference, at small scales, between convective and internal decorrelation times. In the test-field model, Galilean invariance is restored by altering the direct-interaction approximation so that the build-up of triple correlations is determined by an intrinsically Galilean-invariant characteristic time, associated with pressure fluctuations.

The abridged Lagrangian-history direct-interaction approximation (Kraichnan 1966) combines the Galilean-invariance properties of the test-field model with the total absence of arbitrary constants displayed by the direct-interaction approximation. This is achieved at the cost of substantial added complication. We have also compared this approximation with the computer experiments, and

it appears to be fully competitive in accuracy with the test-field model with $\lambda = 1$. Detailed results will be presented in a later paper.

In conclusion, we should like to call attention again to the demonstration in §4 that asymptotic inertial-range power laws cannot be inferred from computer experiments in the wavenumber and Reynolds number ranges considered here. The apparent k^{-4} inertial range exhibited by the computer experiment in figure 6(a) was perfectly mimicked by the results of the test-field model for the same case, despite the fact that the test-field model yields asymptotically a log-corrected k^{-3} inertial range. In contrast, the numerical experiments using the spectral method show a remarkable Reynolds number and truncation independence of the dynamics of the large-scale enstrophy-containing eddies.

REFERENCES

ARAKAWA, A. 1966 Computational design for long-term integration of the equations of motion: two-dimensional incompressible flow. Part 1. *J. Comp. Phys.* **1**, 119–143.

BATCHELOR, G. K. 1969 Computation of the energy spectrum in homogeneous two-dimensional turbulence. High-speed computing in fluid dynamics. *Phys. Fluids Suppl.* II, **12**, II 233–239.

CHARNEY, J. G. 1971 Geostrophic turbulence. *J. Atmos. Sci.* **28**, 1087–1095.

DEEM, G. S. & ZABUSKY, N. J. 1971 Ergodic boundary in numerical simulations of two-dimensional turbulence. *Phys. Rev. Lett.* **27**, 396–399.

FOX, D. G. & ORSZAG, S. A. 1973a Pseudospectral approximation to two-dimensional turbulence. *J. Comp. Phys.* **11**, 612–619.

FOX, D. G. & ORSZAG, S. A. 1973b Inviscid dynamics of two-dimensional turbulence. *Phys. Fluids*, **16**, 169–171.

HEISENBERG, W. 1948 On the theory of statistical and isotropic turbulence. *Proc. Roy. Soc.* A **195**, 402–406.

HERRING, J. R. & KRAICHNAN, R. H. 1972 Comparison of some approximations for isotropic turbulence. In *Lecture Notes in Physics*, vol. 12. *Statistical Models and Turbulence*, pp. 148–194. Springer.

HERRING, J. R., RILEY, J. J., PATTERSON, G. S. & KRAICHNAN, R. H. 1973 Growth of uncertainty in decaying isotropic turbulence. *J. Atmos. Sci.* **30**, 997–1006.

KRAICHNAN, R. H. 1959 The structure of isotropic turbulence at very high Reynolds numbers. *J. Fluid Mech.* **5**, 497–543.

KRAICHNAN, R. H. 1964 Kolmogorov's hypothesis and Eulerian turbulence theory. *Phys. Fluids*, **7**, 1723–1734.

KRAICHNAN, R. H. 1966 Isotropic turbulence and inertial-range structure. *Phys. Fluids*, **9**, 1728–1752.

KRAICHNAN, R. H. 1967 Inertial range in two-dimensional turbulence. *Phys. Fluids*, **10**, 1417–1423.

KRAICHNAN, R. H. 1971a An almost-Markovian Galilean-invariant turbulence model. *J. Fluid Mech.* **47**, 513–524.

KRAICHNAN, R. H. 1971b Inertial-range transfer in two- and three-dimensional turbulence. *J. Fluid Mech.* **47**, 525–535.

KRAICHNAN, R. H. 1973 Test-field model for inhomogeneous turbulence. *J. Fluid Mech.* **56**, 287–304.

LEITH, C. E. 1971 Atmospheric predictability and two-dimensional turbulence. *J. Atmos. Sci.* **28**, 145–161.

LEITH, C. E. & KRAICHNAN, R. H. 1972 Predictability of turbulent flows. *J. Atmos. Sci.* **29**, 1041–1058.

LILLY, D. K. 1971 Numerical simulation of developing and decaying two-dimensional turbulence. *J. Fluid Mech.* **45**, 395–415.

LILLY, D. K. 1972a Numerical simulation studies of two-dimensional turbulence: I. Models of statistically steady turbulence. *Geophys. Fluid Dyn.* **3**, 289–319.

LILLY, D. K. 1972b Numerical simulation studies of two-dimensional turbulence: II. Stability and predictability studies. *Geophys. Fluid Dyn.* **4**, 1–28.

ORSZAG, S. A. 1970 Analytical theories of turbulence. *J. Fluid Mech.* **41**, 363–386.

ORSZAG, S. A. 1971 Numerical simulation of incompressible flows within simple boundaries. I. Galerkin (spectral) representations. *Studies in Appl. Math.* **50**, 293–327.

ORSZAG, S. A. 1974 *Statistical Theory of Turbulence, Les Houches Summer School on Physics*. Gordon & Breach.

ORSZAG, S. A. & PATTERSON, G. S. 1972 Numerical simulation of three-dimensional homogeneous isotropic turbulence. *Phys. Rev. Lett.* **28**, 76–79. (See also 'Numerical simulation of turbulence.' In *Lecture Notes in Physics*, vol. 12, *Statistical Models and Turbulence*, pp. 127–147. Springer.)